A Novel Satellite-Based REM Construction in Cognitive GEO-LEO Satellite IoT Networks

Quynh Tu Ngo, *Senior Member, IEEE,* Beeshanga Jayawickrama, *Senior Member, IEEE,*
Ying He, *Senior Member, IEEE,* Eryk Dutkiewicz, *Senior Member, IEEE*

***Abstract*—The advancement of 6G technology significantly enhances the Internet of Things (IoT) applications, especially in remote areas where traditional cellular infrastructure is not feasible. Satellite communication, a crucial component of 6G, extends IoT connectivity to these underserved regions. In this context, the growing interest in low earth orbit (LEO) satellite communication stems from its recent advancements in offering high data rate services and minimizing service latency. Next-generation LEO satellite systems, with regenerative capabilities, allow for adaptability in bandwidth management and on-board data processing. However, the scarcity of satellite spectrum presents a barrier to the expansion of LEO satellite networks and the development of integrated terrestrial-space infrastructures. To address this challenge, we propose constructing a Radio Environment Map (REM) aboard LEO satellites to opportunistically tap into the unused spectrum of geostationary (GEO) satellites within a cognitive GEO-LEO satellite IoT network. This solution facilitates REM construction through collaboration among neighboring LEO satellites while also considering the frequency reuse scheme of GEO satellites. Our REM construction approach leverages cyclostationary-based sensing at LEO satellites, serving the dual purpose of REM construction and Doppler shift estimation to track multiple GEO frequency signals. Following REM construction, LEO satellites utilize deep learning techniques to predict GEO spectrum occupancy without further sensing, thereby optimizing secondary spectrum utilization of the IoT network. We propose a deep learning neural network architecture based on a sequence-to-sequence model tailored for spectrum prediction at LEO satellites. Simulations demonstrate superior performance in detection probability of the proposed deep learning network compared to convolutional long short-term memory networks, achieving this with lower computational complexity.**

***Index Terms*—Cognitive GEO-LEO satellite IoT networks, LEO spectrum sensing, spectrum access, satellite-based REM, deep learning.**

I. INTRODUCTION

The advancement of sixth-generation (6G) technology significantly enhances the Internet of Things (IoT) applications, especially in remote areas where traditional cellular infrastructure is not feasible. 6G aims to provide ultra-reliable, low-latency communication, massive connectivity, and high data rates, making it ideal for supporting the expansive growth of IoT devices [1]. One of the most transformative aspects of 6G is its integration of satellite and terrestrial networks, a crucial solution that extends IoT connectivity to underserved regions [2]. Satellite communication ensures that remote and inaccessible areas can benefit from advanced IoT applications, bridging the digital divide and enabling innovations in various fields such as agriculture, environmental monitoring, and disaster management. Recently, the domain of low earth orbit (LEO) satellite systems has experienced significant advancements. LEO satellites, equipped with enhanced regenerative capabilities for bandwidth management and on-board data processing, are revolutionizing satellite communication [3]. These advancements enable substantial improvements in data rates and minimize latency, making LEO satellites highly attractive for a wide range of applications [4]. However, as the number of LEO satellites increases, the availability of frequency resources becomes increasingly limited, posing challenges for the development of integrated terrestrial-space networks. In response to this issue, cognitive satellite networks emerge as a solution, enabling LEO satellites to opportunistically utilize the spectrum of geostationary (GEO) satellites when it remains unused. This innovative approach holds the potential to optimize spectrum utilization and enhance the efficiency of satellite communication systems, facilitating seamless integration between terrestrial and space-based infrastructures.

Within cognitive satellite networks, the responsibility of sensing is predominantly delegated to ground-based cognitive nodes, largely owing to the extensive coverage provided by satellites and the ease of deploying them on the ground [5]–[9]. However, this deployment becomes impractical when these ground-based cognitive nodes are IoT users situated in remote areas. For these IoT users to effectively sense GEO satellite signals and relay the sensing results to LEO satellites, they would need to be well-equipped, often requiring high power usage. This requirement contradicts the low power constraints typically associated with IoT users. Additionally, assigning the sensing task to a LEO satellite presents a compelling opportunity to significantly enhance transmission efficiency for secondary IoT users. This improvement arises from the reduction in propagation delay during sensing, as highlighted in [10]. However, when LEO satellites undertake the sensing, they face a significant challenge due to their high orbital speed, which induces the Doppler effect. This effect poses a substantial hurdle for LEO satellites attempting to accurately track the frequency of GEO signals, thereby affecting the precision of spectrum sensing results. Therefore, there is a pressing need to develop a spectrum sensing mechanism specifically tailored

---

The authors are with the School of Electrical and Data Engineering, University of Technology Sydney, Sydney, NSW 2007, Australia (Email: {QuynhTu.Ngo, Beeshanga.Jayawickrama, Ying.He, Eryk.Dutkiewicz}@uts.edu.au).

This work has been supported by the SmartSat CRC, whose activities are funded by the Australian Government's CRC Program.

for LEO satellites within cognitive GEO-LEO satellite IoT networks. This mechanism must reliably detect the spectrum occupancy of GEO satellites while simultaneously tracking multiple frequency channels used by GEO satellites.

In the literature, only studies by [11] and [12] have employed LEO satellites to conduct GEO spectrum sensing. [11] investigates the spectrum sharing challenges in a cognitive satellite network consisting of a GEO satellite and a pair of LEO satellites. One LEO satellite undertakes the task of sensing the usage of the GEO spectrum, while the other LEO satellite engages in secondary transmission utilizing information obtained from the sensing LEO satellite. Despite optimizing the time intervals for spectrum sensing, the transmission protocol employed in [11] introduces additional latency for end-users by separating the sensing and transmission satellites. Furthermore, the optimization problem addressed focuses on maximizing the throughput of the data transmission LEO satellite, overlooking solutions for mitigating Doppler shift resulting from the movement of LEO satellites. On the other hand, [12] proposes a machine learning-based cyclostationary spectrum sensing algorithm tailored for LEO satellites engaged in sensing GEO satellite spectrum activity within a cognitive dual satellite system. Although the proposed sensing algorithm takes into account the Doppler shift experienced by LEO satellites, it falls short in addressing the GEO frequency tracking problem in cognitive GEO-LEO networks. Additionally, the study in [12] solely examines a scenario where the LEO satellite operates under a GEO satellite single beam, which may not align with practical operational conditions.

The Radio Environment Map (REM) technique, renowned for its highly dynamic development and update capabilities, has garnered significant attention and utilization in terrestrial communication contexts. The REM technique can construct the spectrum occupancy database of vast areas with only a few randomly distributed cognitive nodes [13]. This feature is particularly relevant in LEO satellite communication, where the frequent orbital passes of LEO satellites demand a dynamic spectrum database to efficiently manage spectrum resources. The endeavor to construct a REM for GEO satellite frequency usage in cognitive satellite networks has thus far been proposed to be executed with sensing nodes and fusion centers on the ground [14]. Only [15] attempted to construct a REM in a cognitive GEO-LEO network, with LEO satellites conducting the sensing but not making the sensing decision. Instead, LEO satellites transmit the sensing data to a fusion center on the ground to make the sensing decision and construct the REM.

In response to the identified research gap, we propose an innovative protocol for constructing REM directly on LEO satellites. This protocol enables cognitive use of the GEO spectrum within cognitive GEO-LEO satellite IoT networks. To the best of our knowledge, this is the first approach in the literature that constructs a REM on the GEO spectrum entirely using LEO satellites. In our framework, the LEO satellites perform spectrum sensing and address the challenge of tracking GEO frequencies, all while accommodating the GEO frequency reuse scheme.

Our protocol employs cyclostationary-based sensing on LEO satellites, which serves two critical functions: constructing REMs and estimating Doppler shifts. The connection between these functions is crucial for accurate REM construction and efficient spectrum utilization. By estimating Doppler shifts, the LEO satellites can track the rapid frequency changes caused by their high velocity relative to GEO satellites. This Doppler estimation aids in more precise spectrum sensing, ensuring that the REM reflects the true spectral environment, even in the presence of frequency shifts. To further enhance the utility of the constructed REMs, we introduce a deep learning algorithm based on a sequence-to-sequence model for spectrum prediction. This model leverages the historical REM data to predict GEO spectrum availability, allowing secondary LEO satellite IoT networks to operate without continuous spectrum sensing. This integration of spectrum sensing, Doppler shift estimation, and spectrum prediction leads to a significant improvement in the efficiency of secondary spectrum utilization in LEO satellite IoT networks.

The main contributions of this paper are summarized as follows:

- We analyze L-band downlink signals from the GEO satellite Inmarsat-4 F1 at two locations within different spot beams to evaluate spectrum sensing feasibility for LEO satellites, considering Inmarsat's frequency reuse scheme.
- We propose a satellite-based REM construction mechanism adapting to LEO satellite fast movement across GEO beams. The REM is constructed in a distributed manner among LEO satellites, covering a larger area than the required LEO coverage area.
- We introduce a cyclostationary-based detection algorithm for GEO signals, designed for LEO satellites, which estimates Doppler shifts based on GEO signal features to aid spectrum sensing and frequency tracking.
- To improve secondary spectrum utilization in LEO satellite IoT networks, we use REM data to predict GEO beam statuses with a deep learning sequence-to-sequence model, capturing spectral and temporal dependencies without additional sensing.
- Numerical simulations show that the proposed REM construction protocol achieves over 80% detection probability in low signal-to-noise ratio (SNR) regions. Additionally, the prediction algorithm performs 18% better in detection probability compared to convolutional long short-term memory (LSTM) while being ten times more computationally efficient.

The remainder of this paper is organized as follows. Section II assesses the feasibility of conducting spectrum sensing on LEO satellites. Section III describes the system model and introduces the proposed REM construction protocol. In Section IV, we present a cyclostationary-based solution for spectrum sensing and Doppler estimation. Section V elaborates on the proposed deep learning algorithm for spectrum prediction using the constructed REM data. Section VI showcases the numerical results. Finally, Section VII provides concluding remarks.

Notation: $\dot{f}$ denotes the first derivative of f; f^T denotes the transpose of f; $\mathbb{P}$ and $\mathbb{E}$ denote probability and expectation

TABLE I: Summary of notations.

Variable	Description
N	Number of LEO satellites
K	Number of GEO satellite spot beams
M	Number of GEO beams within LEO sensing range
t_L	Duration LEO satellites inside GEO coverage
T_S	Duration of a time-slot
T_{ob}	Number of observation samples of received signal
S	GEO channel state space
s_t	GEO channel state at the t-th time-slot
H	HMM transition matrix
$x(t)$	Signal transmitted by GEO satellite
$n_n(t)$	AWGN at the n-th LEO satellite
$y_{L_n}(t)$	Received signal at the n-th LEO satellite
h_{GL_n}	GEO-LEO channel coefficient
G_{L_n}	Channel gain factor
d_{GL_n}	Distance between GEO and S_{L_n} LEO satellites
f_c	Carrier frequency
f_D/Δ_D	Doppler shift and its rate of change
$\tilde{f}_D/\tilde{\Delta}_D$	Estimated Doppler shift and its rate of change
R_y	Autocorrelation function (ACF) of $y(t)$
R_y^{α}	Cyclic autocorrelation function (CACF) of $y(t)$
$F_{th,\iota}$	Feature threshold for the ι-th subband
κ	Adaptive factor of feature threshold
$\theta(t)$	Elevation angle
$\dot{\psi}(t)$	LEO satellite angular velocity
λ	Noncentrality parameter of Chi-squared distribution
X_t	Input matrix of deep learning neural network
n_b	Number of beams of interest
n_t	Number of historical data
n_{lc}	Number of memory blocks per LSTM unit/layer
l_i	Length of input sequence-LSTM
d_s	State dimension of a LSTM unit/layer
n_{ci}	Number of input channels-CNN
ζ_{ci}	Spacial size of the convolutional kernel
n_{co}	Number of output channels-CNN
ζ_{co}	Spatial size of the output feature map-CNN
n_{sof}	Number of input neurons-Softmax layer
n_{di}/n_{do}	Number of input/output neurons-Dense layer

operations, respectively. The notation used in this paper is summarized in Table I.

II. FEASIBILITY OF SENSING ON LEO SATELLITES

In cognitive GEO satellite networks, the predominant approach involves conducting ground-based sensing of GEO signals. This is primarily driven by the extensive coverage of GEO satellites on the ground, facilitating the deployment of numerous sensor nodes across the GEO coverage area. This method is particularly prevalent in current practices within cognitive satellite networks, especially when building a REM of GEO satellite activities. However, there is ongoing exploration into optimizing sensing locations, particularly concerning the extent of GEO spectrum reuse by LEO satellites [10]. In [10], the impact of propagation delay on sensing location is examined, leading to the conclusion that assigning the sensing task to LEO satellites results in a higher percentage of secondary spectrum usage compared to ground-based sensing in a cognitive GEO-LEO satellite network. Since LEO satellites are only within the coverage range of one GEO spot beam using one frequency subband at a time, they need information on GEO activity in other subbands to build the REM. This knowledge is essential for the feasibility of performing sensing on LEO satellites. To evaluate this feasibility, we captured and analyzed the downlink signals of the GEO satellite Inmarsat-4 F1. This investigation was conducted simultaneously at two distinct locations in Australia: Sydney and Adelaide, each belonging to a different narrowed spot beam within the GEO coverage area as illustrated in Fig. 1a. We employed two universal software radio peripherals that are time and frequency synchronized to the global positioning system, recording raw IQ samples continuously for two hours. Time synchronization was achieved with an accuracy on the order of 50 ns. The measurement platform is described in detail in [16]. Our objective was to explore potential correlations between signals at different beams.

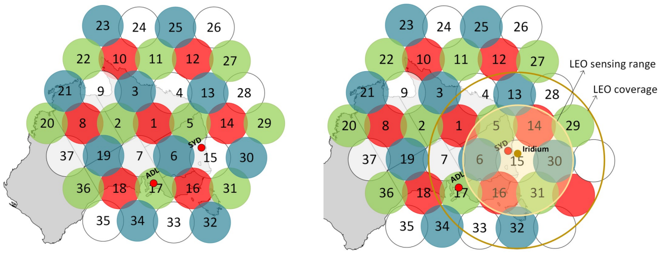

(a) Narrowed spot beam map (b) With Iridium-NEXT 145 beam coverage & sensing range

Fig. 1: Inmarsat-4 F1 beam map over Australia.

The results shown in Fig. 2 indicate that while some signals appear to be present in both beams, the signals detected with a strong power level at Sydney are still being received at Adelaide at a lower power level, and vice versa. Given that Inmarsat-4 F1 utilizes a four-color (4C) frequency reuse scheme [17], we can illustrate an example of the beam color scheme as depicted in Fig. 1. This scheme is a carrier reutilization strategy utilizing a 4C pattern to allocate beams to four subbands, promoting frequency reuse with outstanding interference isolation characteristics [18].

It can be observed that the signal picked up by the Adelaide sensor node in cell 17, is the aggregate signal of cells 7 and 13 in the white color subband. Notably, Sydney also belongs to a white color cell. Similarly, the Sydney sensor node in cell 15 can capture signals from the green color cells 5 and 31, with Adelaide also belonging to a green color beam. Therefore, we can deduce the sensing range is one-hop tier. For instance, if a sensor node is in cell 15, its sensing range encompasses cells 15, 5, 6, 16, 31, 30, and 14.

To assess the sensing range at LEO level, we conducted a simulation of a cognitive network involving the Inmarsat-4 F1 as a primary user (PU) transmitting to one of its users situated in Sydney, while the Iridium-NEXT 145 acted as a secondary user (SU) sensing the PU's transmission. With a transmitted power of 50 dBW from Inmarsat-4 F1, the received signal power at the Iridium-NEXT 145 and the Sydney user measured -125.2805 dBW and -125.5043 dBW, respectively, during the pass of the Iridium satellite over the Sydney user. The ground coverage diameter of an Inmarsat beam is approximately 1110 km, computed using the Haversine formula [19] and referencing the Inmarsat-4 coverage map [20]. At the altitude of Iridium-NEXT 145, this same beam exhibits a diameter of 1085.8 km. Subsequently, we conducted an informed estimation, leading to the deduction that the Iridium-NEXT 145 sensing range is also one-hop tier. The coverage area of an Iridium satellite constitutes a circular region with a diameter of 4700 km [21], encompassing two-hop beams from the central beam where Iridium-NEXT 145 is located.

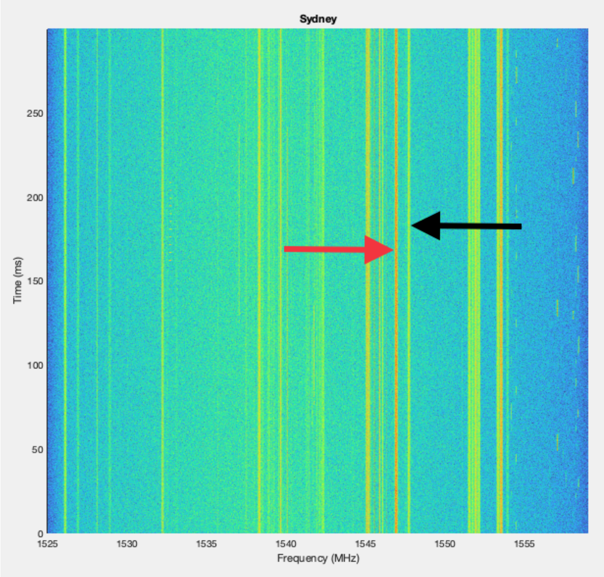

(a) Signals captured at Sydney

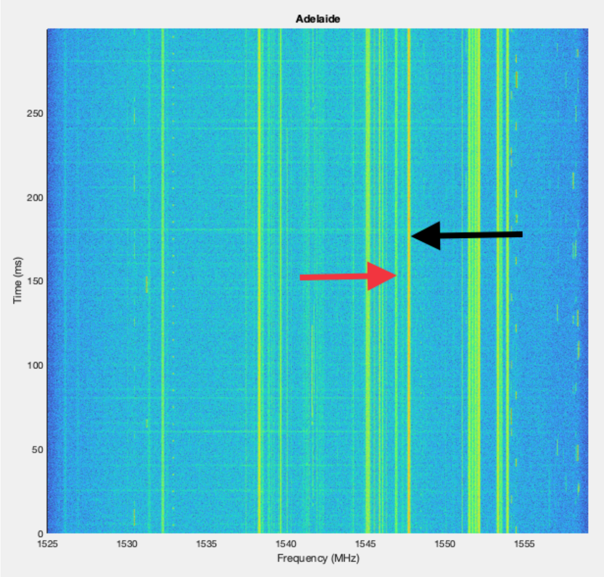

(b) Signals captured at Adelaide

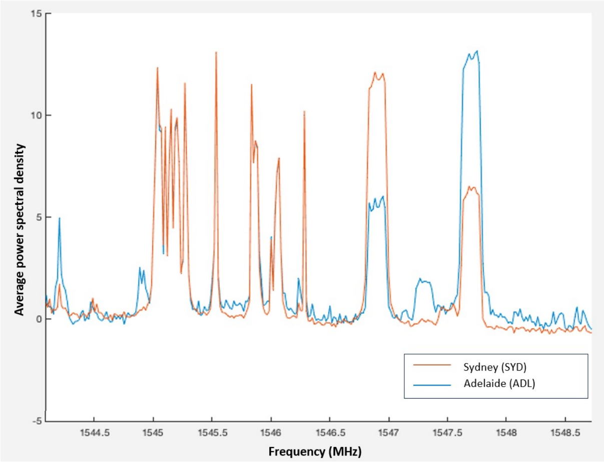

(c) Average power spectral density over time, zoomed into the region of interest

Fig. 2: Inmarsat-4 F1 downlink signals captured at Sydney and Adelaide.

As illustrated in Fig. 1b, when Iridium-NEXT 145 is positioned in cell 15, it has the capability to sense all the one-hop tier cells, while its coverage extends to the two-hop tier. In this scenario, if the Iridium satellite detects an Inmarsat signal within a specific subband, all beams corresponding to that subband become unavailable for secondary transmission. For instance, if Iridium-NEXT 145 is located in a cell marked as white (cell 15) and senses an Inmarsat transmission in the white subband, all other white cells within Iridium-NEXT 145's coverage are considered occupied by Inmarsat. Hence, relying solely on a single LEO satellite for sensing is not efficient in terms of frequency utilization.

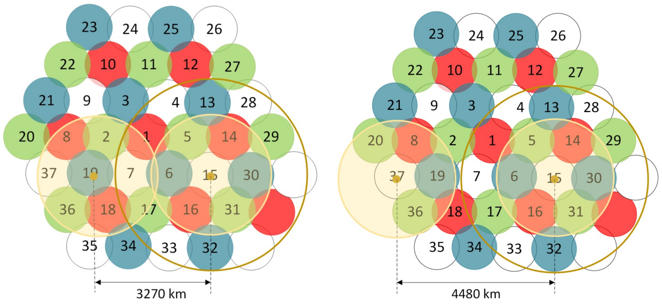

(a) Minimum separation distance (b) Maximum separation distance

Fig. 3: Sensing area of two neighboring Iridium-NEXT satellites.

With each Iridium satellite maintains four inter-satellite links (ISL) with neighboring satellites in the constellation [22], we can enlist the support of these neighboring satellites to sense cells in the two-hop tier of Iridium-NEXT 145. This collaborative sensing approach aims to expand the sensing area from a one-hop tier to a two-hop tier. Within the constellation, the distances between Iridium satellites vary from 3270 km to 4480 km [22]. The sensing range of an Iridium satellite can be elongated to the two-hop tier when the distance from its neighboring Iridium satellites falls within the range of 3270 km to 3370 km, as depicted in Fig. 3.

III. SYSTEM MODEL

We consider a cognitive GEO-LEO satellite IoT network, as illustrated in Fig. 4. In this network, a GEO satellite, designated as S_G, and its users serve as PUs. The GEO satellite utilizes K narrowed spot beams for communication with its users and employs the I-color frequency reuse scheme with $I \in \mathbb{N} | I \geq 1$. Additionally, there is a constellation of N (where $N < K$) LEO satellites, labeled as S_{L_0} to $S_{L_{N-1}}$, which serve their IoT users. These LEO satellite IoT networks operate as the secondary networks opportunistically accessing the GEO downlink spectrum.

The LEO satellites are equipped with multiple antennas, organized into two distinct antenna systems: one system with a

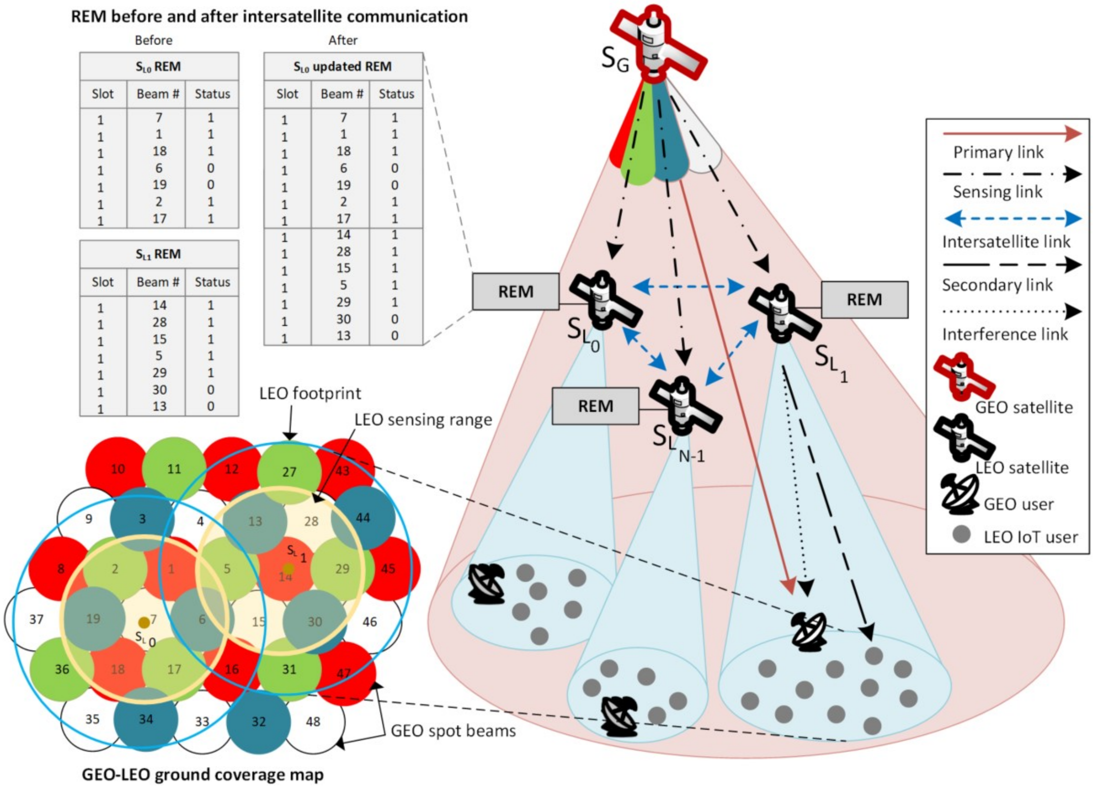

REM before and after intersatellite communication

Before

S_{L0} REM		
Slot	Beam #	Status
1	7	1
1	1	1
1	18	1
1	6	0
1	19	0
1	2	1
1	17	1

S_{L1} REM		
Slot	Beam #	Status
1	14	1
1	28	1
1	15	1
1	5	1
1	29	1
1	30	0
1	13	0

After

S_{L0} updated REM		
Slot	Beam #	Status
1	7	1
1	1	1
1	18	1
1	6	0
1	19	0
1	2	1
1	17	1
1	14	1
1	28	1
1	15	1
1	5	1
1	29	1
1	30	0
1	13	0

Fig. 4: An example of a cognitive GEO-LEO satellite IoT network, where the GEO satellite utilizes a 4-color frequency reuse scheme.

single antenna dedicated to sensing and inter-satellite communications, and another system comprising multiple antennas for satellite-terrestrial communications. Additionally, these LEO satellites are furnished with tunable receivers, enabling them to dynamically adjust their frequencies to receive signals from multiple frequencies used by GEO satellite beams. The LEO satellites are assumed to be perfectly time-synchronized. All LEO satellites engage in spectrum sensing to detect GEO satellite activity. Each LEO satellite senses M beams based on its position and autonomously makes sensing decisions. Subsequently, the LEO satellites share their sensing results via ISLs, which are channels dedicated to control plane communications and have limited bandwidth. During their orbits within the coverage range of the GEO satellite, each LEO satellite accumulates a local REM and subsequently engages in secondary transmissions based on this local REM.

A. Radio environment map construction and usage

Let t_L represent the duration during which LEO satellites are within the coverage range of GEO satellite. This time period, t_L, is subdivided into multiple time-slots, each lasting T_S, as depicted in Fig. 5. The first ζ time-slots are dedicated to the REM construction phase, while the remaining time-slots are used for REM operation without sensing.

During the REM construction phase, each time-slot includes a dedicated sensing and decision window at the beginning. In this window, LEO satellites employ cyclostationary-based sensing [12], which serves two purposes: sensing the GEO spectrum and tracking GEO frequencies. Details on cyclostationary sensing and frequency tracking are provided in Section IV.

Block fading channel model is employed in which the channel gains remain constant within a time-slot but vary between different time-slots [5], [23], [24]. During the sensing and decision windows of each time-slot, all LEO satellites perform multi-band spectrum sensing. They make a binary sensing decision indicating whether a GEO beam is idle (0) or busy (1), and forward this sensing decision to neighbor satellites via ISLs. This single-bit decision reduces control plane overhead and minimizes memory requirements for storing the REM onboard, which is crucial given the limited resources of LEO satellites.

LEO satellites aggregate their own sensing data with information received from neighboring satellites to construct a comprehensive local REM. This aggregated data offers a broader view of beam status beyond each LEO satellite's immediate coverage area. If ISLs are unavailable, each LEO satellite will replicate the sensed statuses of the same subband beams for the two-hop beams.

The channel for secondary transmission is chosen based on the current local REM. Before initiating secondary transmission, the n-th LEO satellite notifies its neighbors of its intention to access the channel. If a beam is selected by multiple LEO satellites for secondary transmission, all satellites will cease transmission in that beam. This alerting process prevents interference in the overlapping coverage regions between neighboring LEO satellites. The detailed process of

REM construction at the n-th LEO satellite is outlined in Algorithm 1, where SR_{14} and TR_{14} represent the sensing range and transmission range, respectively, when the LEO satellite's position is within beam 14.

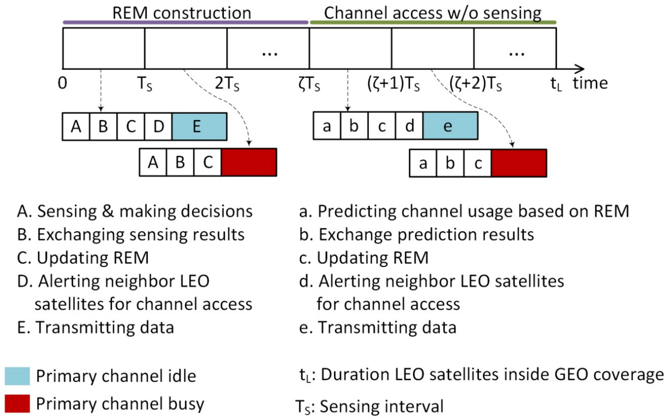

Fig. 5: Timeline for REM construction and usage at a LEO satellite.

Algorithm 1: REM construction protocol at a LEO satellite (S_{L_1})

```
1  Initialization;
2  while true do
3      Get satellite position (i.e., beam 14) and time-slot
         (i.e., $iT_S$);
4      Perform spectrum sensing on $SR_{14}$;
5      Obtain sensing result for all beams in $SR_{14}$;
6      Check for neighboring satellites within a
         predetermined distance and ISLs;
7      if neighbors and ISLs exist then
8          Exchange sensing result of $SR_{14}$ with
             neighbors and receive their SR sensing results;
9      else
10         Achieve sensing result for $TR_{14}$ by setting
             beams in the same subband to have the same
             statuses as those in $SR_{14}$;
11     end if
12     Update REM. Note: if a beam has two statuses,
         record beam status as sensed in $SR_{14}$;
13     Check REM for idle beam(s);
14     if no idle beams then
15         Go back to 3        # Repeat the process;
16     else
17         Exchange beam selection for secondary
             transmission with neighbors. Note: if a beam
             is also selected by neighbors, cease
             transmission in that beam;
18         Perform secondary transmission;
19         Go back to 3        # Repeat the process;
20     end if
21 end while
```

In Fig. 4, consider satellite S_{L_1} within beam 14, which can detect occupancy at the red subband and aggregate signals from the other three colored subbands. It is essential to highlight that beams within the same subband should exhibit identical statuses. Following the sensing and decision-making process, S_{L_1} records the statuses of beams 14, 5, 29, 15, 28, 13, and 30. Subsequently, S_{L_1} shares these sensing results with neighboring satellites through ISLs, establishing its local REM. It is assumed that the beam ID and subband are known between LEO satellites since each LEO satellite is aware of its position, and the beam width at LEO satellite altitude can be treated as an approximately known constant value.

After gathering ample data across ζ time-slots within the REM, when the n-th LEO satellite progresses to a new communication session, involving a different coverage area on the ground as it orbits, the n-th LEO satellite utilizes deep learning technique to predict the status of the emerging GEO beams using the REM data without performing sensing. This approach eliminates the necessity for supplementary sensing, consequently prolonging the duration of secondary spectrum usage. It is important to note that the n-th LEO satellite only predicts the status of the beams within its transmission range, not all the beams in its local REM. Therefore, collaboration with neighboring satellites is required to keep the entire local REM up to date.

B. GEO satellite activity model

A two-state Hidden Markov Model (HMM) is employed to represent the on/off states of GEO satellite activity. Utilizing the HMM offers a key advantage: LEO satellites can acquire training sequences by making repeated visits to the GEO coverage area, even without prior knowledge. Hence, the communication channels between GEO and LEO satellites can be treated as Additive White Gaussian Noise (AWGN) channels with fixed channel gains. For simplicity, we assume the errors in channel estimation are negligible. Let $\mathcal{S} = \{0, 1\}$ represent the state space, where 0 and 1 correspond to the idle and busy states of a GEO satellite downlink channel, respectively. The initial probability distribution of the state is denoted as $\pi = \{\pi_0, \pi_1\}$. The HMM transition matrix can be written as

$$H = \{\mathbb{P}\left(s_{t+1} = j | s_t = i\right)\},\ i, j \in \mathcal{S} \tag{1}$$

where s_t represents the channel state at the t-th time-slot.

C. Satellite signal and channel model

We employ the AWGN channel model to characterize the GEO-LEO links [25]. In this model, we assume that the line-of-sight component of the GEO-LEO links predominantly contributes to the received signals at the LEO satellites. The signal sensed at the n-th LEO satellite S_{L_n} can be expressed as

$$y_{L_n}(t) = h_{L_n}^T x(t) + n_n(t), \quad t = 0, \cdots, T_{ob} - 1 \tag{2}$$

where $h_{L_n} \in \mathbb{C}^{M \times 1}$ denotes the channel vector including the channel coefficients seen by S_{L_n} from all M beams where $\mathbb{C}$ represents the complex-valued matrix space; $x(t)$ represents the GEO signal vector of M symbols, and $n_n \sim \mathcal{CN}\left(0, \sigma_n^2\right)$ with σ_n^2 being the variance of the complex AWGN seen by S_{L_n}; $x(t)$ and $n_n(t)$ are independent and identically distributed (i.i.d.).

The satellite channel coefficient h_{L_n} comprises a path loss factor and a gain factor and can be expressed as

$$h_{L_n} = G_{GL_n} \left(\frac{c}{4\pi f_c d_{GL_n}} \right)^2 . \tag{3}$$

Here, G_{GL_n} represents the gain factor, characterizing the antenna gain at both S_G and S_{L_n} satellites, as well as the amplifier on S_G. c denotes the speed of light, f_c represents the carrier frequency, and d_{GL_n} is the distance between the two satellites. The relative movement between the two satellites makes d_{GL_n} a time-varying distance, thus rendering h_{L_n} a time-varying channel coefficient. Hence, we employ the second-order polynomial phase model to represent h_{L_n}. The received signal in (2) can be written as

$$y_{L_n}(t) = x(t) e^{j\left(2\pi f_D t + \pi \Delta_D t^2\right)} + n_n(t), \tag{4}$$

where f_D and $\Delta_D = \dot{f}_D$ denote the Doppler shift and its rate of change, respectively.

IV. Spectrum Sensing at LEO satellites

Due to the typical non-regenerative nature of GEO satellites, GEO signals primarily consist of relayed signals from Earth stations, which are often non-stationary signals. For instance, signals from systems like Inmarsat employ modulation schemes such as quadrature phase shift keying (QPSK) or quature amplitude modulation (QAM) [26]. Consequently, within the proposed scheme, all LEO satellites utilize feature detection as part of the spectrum sensing process during the REM construction phase. Cyclostationary detection is particularly advantageous in this context due to its ability to exploit the inherent periodicities in modulated signals, such as those found in QPSK or 16-QAM. Unlike energy detection methods that are prone to noise and interference, cyclostationary detection can differentiate between signal and noise based on cyclic frequencies, providing higher sensitivity and reliability in identifying signals even in low SNR environments [12]. This makes it especially effective in non-stationary signal environments typically encountered with GEO satellite transmissions. The main principle of cyclostationary detection involves analyzing the cyclic autocorrelation function of the received signal. By identifying cyclic frequencies, which are unique to certain modulation schemes, the detector can recognize the presence of specific signals amidst noise and interference. The signal characteristics identified during spectrum sensing can also serve the purpose of estimating Doppler shifts for GEO frequency tracking, further enhancing the performance of the LEO satellite system.

A. Cyclostationary-based detection of GEO signals

Due to the I-color frequency reuse scheme employed by GEO satellite, although a LEO satellite senses M GEO beams, it effectively discerns GEO activity across I distinct subbands. Consequently, the spectrum sensing problem for the n-th LEO satellite, determining whether the ι-th subbands ($\iota = 1, \cdots, I$) is occupied or not during the t-th time-slot, can be expressed as a hypothesis testing problem:

$$r_n^{(m)}(t) = \begin{cases} n_n(t), & \mathcal{H}_{0,m} \\ y_{L_n}(t), & \mathcal{H}_{1,m} \end{cases} \qquad t = 0, \cdots, T_{ob} - 1 \tag{5}$$

where $\mathcal{H}_{0,m}$ and $\mathcal{H}_{1,m}$ respectively represent the absence and presence of GEO activity in the ι-th subband.

1) Feature extraction: To simplify the notation, we will use $y(t)$ to represent $y_{L_n}(t)$ in this section. Let us provide a brief introduction to the concept of cyclostationary processes. A general non-stationary signal $y(t)$ is referred to as a second-order cyclostationary signal if its time-varying correlation exhibits (almost) periodic behavior [27]. The time-varying correlation of $y(t)$ is referred to as the autocorrelation function (ACF) and is defined as $R_y(t,\tau) \triangleq \mathbb{E}\{y(t)y^*(t+\tau)\}$. The coefficients in the Fourier series expansion of $R_y(t,\tau)$ are called the cyclic autocorrelation function (CACF),

$$R_y^\alpha(\alpha,\tau) = \frac{1}{T_{ob}} \sum_{t=0}^{T_{ob}-1} R_y(t,\tau) e^{-j\alpha t}, \tag{6}$$

where α represents the cyclic frequency and τ is a time lag.

With $y(t)$ given in (4), its ACF can be expressed as

$$R_y\left(t,\tau\right) = R_x\left(\tau\right) e^{-j\pi\left(2f_D\tau + \Delta_D\tau^2\right)} e^{-2j\pi\Delta_D t\tau} + \sigma_n^2, \tag{7}$$

where $R_x(\tau)$ represents the ACF of $x(t)$. The corresponding CACF can be given as

$$R_y^\alpha(\alpha,\tau) = \frac{2\pi}{T_{ob}} R_x(\tau) e^{j\pi\left(2f_D\tau + \Delta_D\tau^2\right)} \delta\left(\alpha + 2\pi\Delta_D\tau\right) + \frac{2\pi}{T_{ob}} \sigma_n^2 \delta(\alpha), \tag{8}$$

where $\delta(\cdot)$ is the Dirac Delta function.

In our previous work [12], we conducted an ACF and CACF analysis for GEO signals modulated using QPSK. Now, our focus shifts to computing the ACF and CACF for the case where $x(t)$ is a 16-QAM signal. Let us express $x(t) = A_{ij} e^{j\left(2\pi f_c t + \phi_{ij}\right)}$, where A_{ij} represents the complex amplitude for the i-th amplitude level and the j-th phase level, and ϕ_{ij} represents the instantaneous phase corresponding to the 16 different 16-QAM symbols. These variables A_{ij} and ϕ_{ij} are uniformly distributed over the interval $[A_{\min}, A_{\max}]$ and $[0, 2\pi]$, respectively, as part of the 16-QAM modulation scheme. The ACF of $x(t)$ can be written as

$$R_x^{\text{16QAM}}(\tau) = \frac{1}{4}\left(A_{\max}^2 + A_{\min}^2\right) \delta_{ik}\delta_{jl}, \tag{9}$$

where δ_{ik} and δ_{ik} are the Kronecker delta, which is 1 if $i = k$ and $j = l$, and 0 otherwise. The Kronecker delta ensures that the ACF is non-zero only when $i = k$ and $j = l$, corresponding to the same symbol. Equations (7) and (9) reveal that the ACF of $y^{\text{16QAM}}(t)$ exhibits almost periodic behavior in the time domain when τ is held constant. Consequently, $y^{\text{16QAM}}(t)$ qualifies as a second-order cyclostationary signal, and its CACF can be computed as in (8).

2) GEO frequency tracking: It can be observed from (8) that the CACF $R_y^\alpha(\alpha,\tau)$ peaks at $\alpha = -2\pi\Delta_D\tau$ and 0. Therefore, by examining the nonzero peak of the CACF of the received signal, we can estimate the Doppler rate of change Δ_D. In practical scenarios where finite data samples are available, we achieve the CACF using the Short-Time Fourier Transform (STFT),

$$\tilde{R}_y^{\alpha}(\alpha, \tau, w) = \frac{1}{T_{ob}} \sum_{t=0}^{T_{ob}-1} R_y(t + wH, \tau) W(t) e^{-j\alpha t}, \quad (10)$$

where $\tilde{R}_y^{\alpha}(\alpha, \tau, w)$ is the estimated CACF within the w-th time window at cyclic frequency α, w is the time index representing the window number, H is the hop size representing the overlap between consecutive time windows, and $W(\cdot)$ is the window function applied to each segment of the ACF. The Doppler rate of change estimator can be given as

$$\tilde{\Delta}_D = -\frac{1}{2\pi\tau} \arg\max_{\alpha} |\tilde{R}_y^{\alpha}(\alpha, \tau, w)|. \quad (11)$$

Using the estimated $\tilde{\Delta}_D$, we can demodulate the signal $y(t)$ as described in (2), effectively reducing the polynomial order to the first order,

$$\begin{aligned} \tilde{y}(t) &= \left(x(t) e^{j\left(2\pi f_D t + \pi \Delta_D t^2\right)} + n_n(t) \right) \times e^{-j\pi\Delta_D t^2} \\ &= x(t) e^{j2\pi f_D t} + n(t) e^{-j\pi\Delta_D t^2}. \end{aligned} \quad (12)$$

The estimation of f_D can now be based on the value of α for which the cyclic first moment of $\tilde{y}(t)$ is nonzero [28]. The cyclic first moment of $\tilde{y}(t)$ can be expressed as

$$\begin{aligned} R_{\tilde{y}}^{\alpha}(\alpha) =& \frac{1}{T_{ob}} \sum_{t=0}^{T_{ob}-1} \mathbb{E}\{\tilde{y}(t)\} e^{-j\alpha t} \\ =& \frac{2\pi}{T_{ob}} \mathbb{E}\{x(t)\} \delta\left(\alpha - 2\pi f_D\right). \end{aligned} \quad (13)$$

Similar to (10), we employ STFT to estimate the cyclic first moment $\tilde{R}_{\tilde{y}}^{\alpha}(\alpha, w)$. The Doppler shift estimator can be given as

$$\tilde{f}_D = \frac{1}{2\pi} \arg\max_{\alpha} |\tilde{R}_{\tilde{y}}^{\alpha}(\alpha, w)|. \quad (14)$$

After estimating the Doppler effect in the received signal, we can implement Doppler compensation using the Phase-Locked Loop (PLL) method, as outlined in [29]. The PLL-based Doppler compensation system is capable of effectively compensating for Doppler frequencies as high as ±200 kHz.

3) Sensing decision: Let $\hat{R}_y^{\alpha}(\alpha, \tau)$ represent the CACF of the received signal after Doppler compensation. To make a decision in spectrum sensing, we compare the feature value $|\hat{R}_y^{\alpha}|^2$ against a predefined threshold. Consequently, the hypothesis testing problem described in (5) can be reformulated as follows:

$$|\hat{R}_y^{\alpha}(\alpha, \tau)|^2 \underset{\mathcal{H}_{0,\iota}}{\overset{\mathcal{H}_{1,\iota}}{\gtrless}} F_{th,\iota}, \quad (15a)$$

$$F_{th,\iota} = \kappa |\max\{\hat{R}_y^{\alpha}\}|^2, \quad (15b)$$

where $F_{th,\iota}$ represents the feature threshold for the ι-th sub-band and κ is the adaptive factor.

B. Performance evaluation

When the LEO satellite detects the spectrum, it typically encounters two types of sensing errors. The first type is a false alarm, occurring when the LEO satellite perceives the channel as occupied when, in reality, it is unoccupied. The second type is termed misdetection, signifying the scenario in which the LEO satellite fails to detect the presence of GEO satellite transmission. Before delving into these two types of sensing errors, we first characterize the Doppler shift.

1) Doppler shift characterization: We consider the Earth-Centered Fixed (ECF) frame in this section. It is assumed that the LEO satellite's orbit, concerning its visibility window with respect to GEO satellite, is approximated as a circular arc. This assumption implies that the LEO orbit is treated as circular, exhibiting zero eccentricity.

The Doppler shift is defined as

$$f_D = -\frac{f_c}{c} \dot{d}_{GL}(t). \quad (16)$$

Fig. 6 illustrates the satellite geometry, where $\theta(t)$ represents the elevation angle from the LEO satellite to the GEO satellite, and $\gamma(t)$ denotes the central angle between their positions. Based on Fig. 6a, the distance between two satellites can be expressed as

$$d_{GL}(t) = \sqrt{R_L^2 + R_G^2 - 2R_L R_G \cos\gamma(t)}, \quad (17)$$

where $R_L = R_E + h_L$ and $R_G = R_E + h_G$, with R_E being the Earth radius, h_L and h_G representing the altitudes of the LEO and GEO satellites, respectively.

Let t_0 denote the instant when LEO satellite observes maximum elevation angle. The angular distance between S_L and S_L' is represented by $\psi(t) - \psi(t_0)$, as shown in Fig. 6b, in which A is the intersection point between OS_G and the LEO satellite orbit spherical plane. By invoking the cosine law of sides applied to the spherical right triangle $S_L A S_L'$, we obtain

$$\cos\gamma(t) = \cos\left(\psi(t) - \psi(t_0)\right) \cos\gamma(t_0). \quad (18)$$

From the triangle plane $S_G O S_L'$ similar to Fig. 6a, we have

$$\cos\gamma(t_0) = \cos\left(\cos^{-1}\left(\frac{R_L}{R_G} \cos\theta_{\max} \right) - \theta_{\max} \right), \quad (19)$$

where $\theta_{\max} = \theta(t_0)$ is the maximum elevation angle. Differentiating (17) and (18) results

$$\dot{d}_{GL}(t) = \frac{R_L R_G \sin\gamma(t) \dot{\gamma}(t)}{\sqrt{R_L^2 R_G^2 - 2R_L R_G \cos\gamma(t)}}, \quad (20)$$

where $\dot{\gamma}(t)$ represents the rate of change of central angle between the positions of the GEO and LEO satellites,

$$\dot{\gamma}(t) = \frac{\dot{\psi}(t) \cos\gamma(t_0) \sin\left(\psi(t) - \psi(t_0)\right)}{\sqrt{1 - \cos^2\left(\psi(t) - \psi(t_0)\right) \cos^2\gamma(t_0)}}, \quad (21)$$

with $\dot{\psi}(t)$ being the LEO satellite angular velocity.

Substituting (20) into (16) and using the relation $\cos\theta(t) = R_G \sin\gamma(t) / d_{GL}(t)$ [30, eq.(3-4)], we arrive at the expression for Doppler shift,

$$f_D = -\frac{f_c R_L}{c} \dot{\gamma}(t) \cos\theta(t). \quad (22)$$

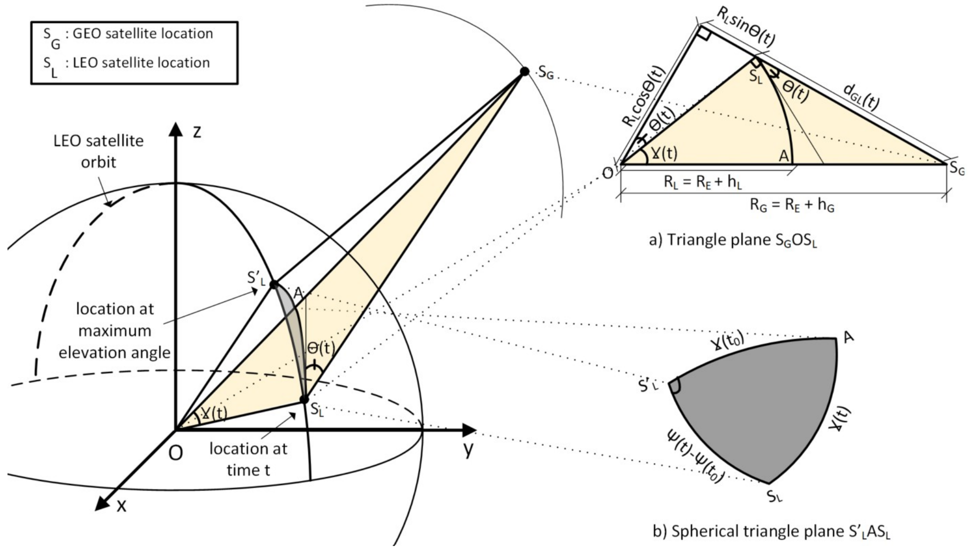

a) Triangle plane S_GOS_L

b) Spherical triangle plane S'_LAS_L

Fig. 6: Illustration of the geometry between GEO and LEO satellites during the LEO satellite's orbit.

Lemma 1. *With a maximum elevation angle* $\theta_{\max} \in \left(0, \frac{\pi}{2}\right)$*, the Doppler shift in (22) has the following upper bound,*

$$f_D^{ub} = -\frac{f_c R_L}{c}\omega_L \cos\theta(t), \tag{23}$$

where $\omega_L = \dot{\psi}(t)$ *is the LEO satellite angular velocity (rad/s) in the ECF frame.*

Proof. When considering fixed R_L and R_G, $\cos\gamma(t_0)$ in (19) is an increasing function of $\theta_{\max}$. For $\theta_{\max} \in \left[0, \frac{\pi}{2}\right]$, $\cos\gamma(t_0) \in \left[\frac{R_L}{R_G}, 1\right]$. Hence, for $\theta_{\max} \in \left(0, \frac{\pi}{2}\right)$, $\cos\gamma(t_0) < 1$. In (21), we have $\frac{\left|\sin\left(\psi(t)-\psi(t_0)\right)\right|}{\sqrt{1-\cos^2\left(\psi(t)-\psi(t_0)\right)\cos^2\gamma(t_0)}} < 1$ for $0 < \cos\gamma(t_0) < 1$, leading to $\dot{\gamma}(t) < \omega_L$, and consequently, establishing the upper bound of Doppler shift. □

The CACF of the received signal after Doppler compensation, hence, can be expressed as:

$$\begin{aligned}\hat{R}_y^{\alpha}(\alpha,\tau) =& \frac{2\pi}{T_{ob}} R_x(\tau) e^{j\pi\left(2\left(f_D-\tilde{f}_D\right)\tau + \left(\Delta_D - \tilde{\Delta}_D\right)\tau^2\right)} \\ & \times \delta\left(\alpha + 2\pi\left(\Delta_D - \tilde{\Delta}_D\right)\tau\right) + \frac{2\pi}{T_{ob}}\sigma_n^2\delta(\alpha),\end{aligned} \tag{24}$$

where $\left(f_D - \tilde{f}_D\right)$ and $\left(\Delta_D - \tilde{\Delta}_D\right)$ represent the Doppler residuals, which follow a Gaussian distribution [31].

2) False alarm probability: Under the $\mathcal{H}_{0,\iota}$ hypothesis, the false alarm (FA) probability for the ι-th subband is defined as

$$P_{fa}^{(\iota)} = 1 - \mathbb{P}\left\{|\hat{R}_y^{\alpha}(\alpha,\tau)|^2 < F_{th,\iota}|\mathcal{H}_{0,\iota}\right\}. \tag{25}$$

Under the $\mathcal{H}_{0,\iota}$ hypothesis, $\hat{R}_y^{\alpha}(\alpha,\tau)|\mathcal{H}_{0,\iota}$ can be considered a zero-mean Gaussian random variable, given that $n_n(t)$ is a zero-mean Gaussian random variable with variance σ_n^2. The variance of $\hat{R}_y^{\alpha}(\alpha,\tau)|\mathcal{H}_{0,\iota}$ is expressed as

$$\text{var}\left\{\hat{R}_y^{\alpha}(\alpha,\tau)|\mathcal{H}_{0,\iota}\right\} = 2\left(\frac{2\pi}{T_{ob}}\sigma_n^2\right)^2. \tag{26}$$

Given that $\hat{R}_y^{\alpha}(\alpha,\tau)|\mathcal{H}_{0,\iota}$ follows a complex Gaussian distribution, its squared magnitude can be represented by a Chi-squared random variable, χ^2, with two degrees of freedom. Let $\tilde{r}_y$ represent $|\hat{R}_y^{\alpha}(\alpha,\tau)|^2$, its probability density function (PDF) is given by

$$f\left(\tilde{r}_y\right) = \frac{T_{ob}^2}{16\pi^2\sigma_n^4} e^{-\frac{\tilde{r}_y T_{ob}^2}{16\pi^2\sigma_n^4}}. \tag{27}$$

The FA probability is resulted as

$$\begin{aligned} P_{fa}^{(\iota)} &= 1 - \mathbb{P}\left\{|\hat{R}_y^{\alpha}(\alpha,\tau)|^2 < F_{th,\iota}|\mathcal{H}_{0,\iota}\right\} \\ &= 1 - \int_0^{F_{th,m}} f_{\tilde{r}_y|\mathcal{H}_{0,\iota}}\left(\tilde{r}_y\right) d\tilde{r}_y \\ &= 1 - \frac{16\pi^2\sigma_n^4}{T_{ob}^2}\left(1 - e^{\frac{-F_{th,\iota}T_{ob}^2}{16\pi^2\sigma_n^4}}\right). \end{aligned} \tag{28}$$

With the feature threshold vector $\mathbf{F}_{th} = [F_{th,1}, \cdots, F_{th,x}]^T$, the FA probabilities of all beams can be presented compactly as

$$\mathbf{P}_{fa}\left(\mathbf{F}_{th}\right) = \left[P_{fa}^{(1)}, \cdots, P_{fa}^{(x)}\right]^T. \tag{29}$$

3) Misdetection probability: Misdetection probability is the compliment of the detection probability. The detection probability for the ι-th subband is considered under the $\mathcal{H}_{1,\iota}$ hypothesis, defined as

$$P_d^{(\iota)} = \mathbb{P}\left\{|\hat{R}_y^{\alpha}(\alpha,\tau)|^2 > F_{th,\iota}|\mathcal{H}_{1,\iota}\right\}. \tag{30}$$

The detection probability is

$$\begin{aligned} P_d^{(\iota)} &= \mathbb{P}\left\{|\hat{R}_y^{\alpha}(\alpha,\tau)|^2 > F_{th,\iota}|\mathcal{H}_{1,\iota}\right\} \\ &= \int_{F_{th,\iota}}^{\infty} g_{\tilde{r}_y|\mathcal{H}_{1,\iota}}\left(\tilde{r}_y\right) d\tilde{r}_y \end{aligned} \tag{31}$$

where $g\left(\tilde{r}_y\right)$ denotes the PDF of $\tilde{r}_y = |\hat{R}_y^{\alpha}(\alpha,\tau)|^2|\mathcal{H}_{1,\iota}$.

According to the Central Limit Theorem, when the sum of numerous i.i.d. random variables is considered, assuming that the sum has a finite variance, the distribution of this sum converges to a Gaussian distribution as the number of random variables becomes sufficiently large. Therefore, $y_{L_n}(t)$ tends to have an approximately Gaussian distribution. With $\hat{R}_y^{\alpha}(\alpha,\tau)|\mathcal{H}_{1,\iota}$ as in (24), we have

$$\begin{aligned}\mathbb{E}\left\{\hat{R}_y^{\alpha}(\alpha,\tau)|\mathcal{H}_{1,\iota}\right\} =& \frac{2\pi}{T_{ob}}\mathbb{E}\left\{R_x(\tau)\right\} e^{j\pi\left(2\mathbb{E}\left\{f_D-\tilde{f}_D\right\}\tau+\mathbb{E}\left\{\Delta_D-\tilde{\Delta}_D\right\}\tau^2\right)} \\ &\times \mathbb{E}\left\{\delta\left(2\pi\left(\Delta_D-\tilde{\Delta}_D\right)\tau\right)\right\} + \frac{2\pi}{T_{ob}}\sigma_n^2 \neq 0.\end{aligned} \tag{32}$$

Remark 1. *With* $\hat{R}_y^{\alpha}(\alpha,\tau)|\mathcal{H}_{1,\iota}$ *is a Gaussian random variable, its squared magnitude can be represented by a noncentral Chi-squared random variable with two degrees of freedom with the PDF expressed as follows*

$$g(\tilde{r}_y) = \frac{1}{2\lambda}e^{-(\tilde{r}_y+\lambda)/2}I_{-1}\left(\sqrt{\lambda\tilde{r}_y}\right), \tag{33a}$$

$$\lambda = \frac{4\pi^2}{T_{ob}^2}\left(\mathbb{E}\left\{|R_x(\tau)|^2\right\}+\sigma_n^4-2\right), \tag{33b}$$

where $I_{-1}(\cdot)$ *denotes the modified Bessel function of the first kind.*

Proof. First, we demonstrate that $\hat{R}_y^{\alpha}(\alpha,\tau)|\mathcal{H}_{1,\iota}$ is a Gaussian random variable. It is evident from (24) that the exponential term involves Gaussian-distributed variables (the Doppler residuals). As $\hat{R}_y^{\alpha}(\alpha,\tau)$ is a linear combination of Gaussian variables (σ_n^2, Gaussian Doppler residuals) and deterministic coefficients, it is inherently a Gaussian random variable. Note that the Dirac delta functions impose specific conditions that further shape the distribution.

For a noncentral Chi-squared distribution with two degrees of freedom, the expectation is given by

$$\mathbb{E}\left\{\tilde{r}_y\right\} = 2+\lambda, \tag{34}$$

where λ is the noncentrality parameter.

With $\hat{R}_y^{\alpha}$ expressed as in (24), the expectation of $\tilde{r}_y = |\hat{R}_y^{\alpha}|^2$ is computed as

$$\mathbb{E}\left\{\tilde{r}_y\right\} = \frac{4\pi^2}{T_{ob}^2}\mathbb{E}\left\{|R_x(\tau)|^2\right\}+\frac{4\pi^2}{T_{ob}^2}\sigma_n^4. \tag{35}$$

From (34) and (35), the PDF results as in (33). □

Thus, the detection probability results as

$$P_d^{(\iota)} = \frac{1}{2}Q_1\left(\sqrt{\lambda},\sqrt{\lambda F_{th,\iota}}\right), \tag{36}$$

where $Q_1(\cdot)$ denotes the first-degree Marcum Q-function.

With the feature threshold vector $\mathbf{F}_{th}$, the misdetection probabilities of all the beams are given by

$$\mathbf{P}_m\left(\mathbf{F}_{th}\right) = \mathbf{1}-\mathbf{P}_d\left(\mathbf{F}_{th}\right), \tag{37}$$

where $\mathbf{1}$ is an all-one vector and $\mathbf{P}_d\left(\mathbf{F}_{th}\right)$ is the vector representation of the detection probability of all beams.

V. REM-BASED SPECTRUM PREDICTION

A. Problem formulation

In this phase, the anticipation of spectrum occupancy relies entirely on the local REM data at the n-th LEO satellite. The predictive algorithm only forecast the status of all GEO beams within the coverage of the n-th LEO satellite, excluding the status of all beams in its local REM to conserve processing time and resources. It is important to highlight that, during this phase, collaborative input from neighboring LEO satellites is indispensable to keep the REM up to date.

To handle the rapid movement of LEO satellites, the deep learning-based spectrum prediction model is designed with adaptability in mind. The model leverages historical REM data, which includes Doppler shift-adjusted spectrum information, enabling it to make accurate predictions even as the satellite environment changes quickly. By continuously adapting to the dynamic conditions of the satellite's orbit and the corresponding frequency shifts, the model ensures reliable spectrum prediction, enhancing the overall efficiency of spectrum management in this rapidly evolving environment.

The spectrum occupancy prediction relies on correlation over time and frequency, as the GEO satellite utilizes the I-color frequency reuse scheme. Therefore, the prediction requires a two-dimensional data approach. An example of two-dimensional data for spectrum prediction for the time-slot ζT_S at satellite S_{L_1} is illustrated in Fig. 7. The input matrix dimension, denoted as $X_t \in \mathbb{B}^{n_b\times n_t}$ where $\mathbb{B}$ represents the space of Boolean values with 0 and 1 indicating idle and busy slots respectively, signifies the number of beams of interest (n_b) and the number of historical time-slots (n_t) we consider as data. The value of n_b depends on the number of beams within the transmission range of the LEO satellite, while n_t is based on the temporal correlation of the input data. We approach the spectrum occupancy prediction as a sequence-to-sequence (SEQ2SEQ) prediction problem, with the input being multiple n_b sequences with length n_t and the output being the occupancy prediction of these n_b sequences.

The SEQ2SEQ neural network is an encoder-decoder architecture where the encoder encodes input data through a series of nonlinear transformations into an intermediate vector, serving as a bridge for subsequent processing. The decoder then decodes the intermediate vector. Originally, both the encoder and decoder in the SEQ2SEQ network were constructed with multiple layers of recurrent neural network (RNN) [32], later improved to incorporate multiple layers of LSTM to address the inherent issues of gradient disappearance and explosion in RNN [33]. An alternative approach involves using a SEQ2SEQ network with gated recurrent unit (GRU) for SEQ2SEQ network [34]. While GRU has a simpler architecture compared to LSTM, it may not perform as well as LSTM in tasks requiring explicit long-term memory retention. In the context of our spectrum occupancy prediction problem, to better capture the complex dynamics of GEO spectrum usage across multiple beams, we propose an SEQ2SEQ network based on LSTM for the spectrum prediction.

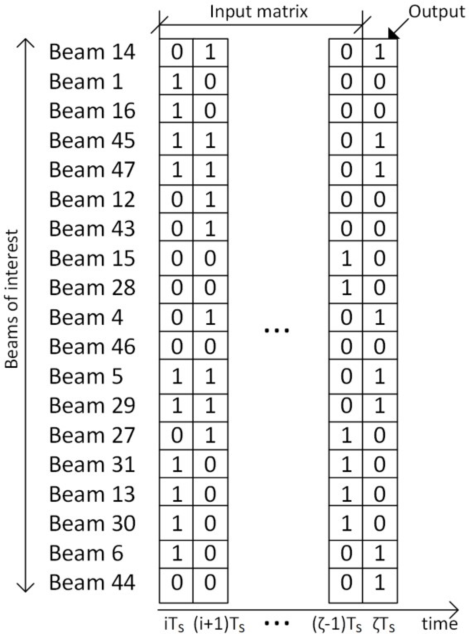

Fig. 7: Data used for spectrum prediction.

B. Proposed multiple beam sequence-to-sequence spectrum prediction network

The proposed SEQ2SEQ network architecture, illustrated in Fig. 8, comprises a bidirectional encoder and decoder, with a softmax layer serving as the bridge for processing between them.

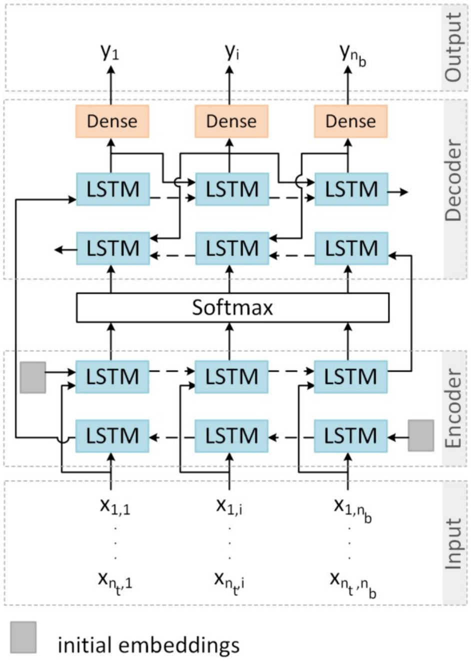

Fig. 8: Proposed SEQ2SEQ network architecture.

The input matrix X_t is divided into n_b sequences, each with a length of n_t, and then passed to the encoder. The encoder is composed of two stacked LSTM layers, with each layer containing n_b LSTM units. Each LSTM unit has n_{lc} memory blocks. In this architecture, bidirectional LSTM is employed, allowing input sequences to be processed by LSTM units in both forward and backward directions. Each LSTM memory block includes at least one cell with a recurrent self-connection, facilitated by gates that enable selective storage, updating, or retrieval of information.

The softmax layer positioned between the encoder and decoder does not aim to encode the input into a fixed-length vector, as typically seen in traditional SEQ2SEQ networks. Instead, it represents a sequence of vectors intended for decoding purposes.

The decoder mirrors the structure of the encoder, comprising two stacked LSTM layers. After the bidirectional LSTM, a dense layer with sigmoid activation for binary classification is present, followed by the output layer. The input to the first LSTM layer in the decoder consists of output sequences from the encoder passed through the softmax layer. Each LSTM layer in the decoder processes these sequences to generate output sequences, benefiting from considering both past and future information due to the bidirectional nature of the LSTM layers. Subsequently, the output sequences pass through a dense layer with sigmoid activation for binary classification, and finally, the output layer produces the final outputs based on the processed information from the LSTM layers and the dense layer.

1) Computational complexity analysis: In this section, we delve into the complexity analysis of the proposed SEQ2SEQ model and the benchmark 2DCNNLSTM [35]. On spectrum prediction network for two-dimensional data, [35] introduced a convolutional LSTM neural network, referred to as 2DCNNLSTM. We adopt 2DCNNLSTM architecture as a baseline to compare with our proposed SEQ2SEQ network. The 2DCNNLSTM network features a 2D convolutional layer with ReLU activation to analyze spectral and temporal correlations. The output is then flattened and reshaped into a 3D tensor, compatible with the LSTM layer, through a Dense layer operating on the temporal dimension. Two LSTM layers are included to capture temporal dependencies, followed by a sigmoid-activated output layer for beam bin predictions. Throughout this section, notations with superscript $\cdot^{SE}$ denote aspects related to SEQ2SEQ, while those with superscript $\cdot^{CL}$ pertain to 2DCNNLSTM.

Let n_{lc}, l_i, and d_s represent the number of memory blocks, the length of input sequence, and the state dimension of a LSTM layer/unit, respectively. Each LSTM layer has the complexity of $\mathcal{O}\left(n_{lc}(l_i+1)\left(d_s n_{lc}/64+n_{lc}\right)\right)$. Let n_{ci} represent the number of input channels, ζ_{ci} denote the spatial size of the convolutional kernel, n_{co} indicate the number of output channels, and ζ_{co} represent the spatial size of the output feature map for a convolutional layer. The computational complexity of a convolutional layer can be expressed as $\mathcal{O}\left(n_{ci}\zeta_{ci}^2 n_{co}\zeta_{co}^2\right)$. A softmax layer with n_{sof} input neurons has a computational complexity of $\mathcal{O}\left(n_{sof}\right)$. A dense layer with n_{di} input neurons and n_{do} output neurons has a computational complexity of $\mathcal{O}\left(n_{di}n_{do}\right)$. The complexity of flatten layer is negligible.

The computational complexity of the proposed scheme and benchmark result as

$$C^{SE} = \mathcal{O}\Bigg(2n_b n_{lc}^{SE}\left(3d_s^{SE}+n_t+2\right)\left(\frac{d_s^{SE}n_{lc}^{SE}}{64}+n_{lc}^{SE}\right) + 2n_b d_s^{SE}\Bigg), \tag{38a}$$

$$C^{CL} = \mathcal{O}\Bigg((n_t+1)\left(\frac{d_s^{CL}}{64}+1\right)\left(\left(n_{lc_1}^{CL}\right)^2+\left(n_{lc_2}^{CL}\right)^2\right) + n_b^2\left(n_t^2\zeta_{ci}^2 n_{co}+n_t+\frac{d_s^{CL}}{n_b}\right)\Bigg). \tag{38b}$$

2) Feasibility of on-board real-time execution: Recent advancements in on-board processing capabilities of LEO satellites have greatly enhanced the feasibility of executing deep learning algorithms in real time. On-orbit experiments have demonstrated the ability of these satellites to perform complex computational tasks, proving that high-performance and reliable on-board processing can be achieved even with limited resources and in harsh space environments [36]. Organizations like NASA and industry leaders have successfully implemented these capabilities in small satellites. For instance, a small LEO satellite equipped with an Intel Tiger Lake UP3 SoC, featuring 4 cores/8 threads and an integrated GPGPU with 96 Execution Units, supported by 4 GB of memory, can provide a robust computational environment suitable for handling moderately complex deep learning tasks [37].

The proposed SEQ2SEQ model, featuring encoder-decoder architecture with LSTM layers, is optimized for low computational complexity. With a matrix of one-bit beam statuses as input and a one-bit array as output, the model minimizes both memory usage and processing time. Despite the resource demands of LSTM networks, which require maintaining and updating cell states, the model's design ensures a balance between accuracy and computational efficiency due to its relatively simple input-output structure.

A LEO satellite equipped with a multi-core CPU, Intel Tiger Lake UP3 SoC and an integrated GPGPU with 96 Execution Units, is well-suited for the parallel processing demands of deep learning inference. This hardware can accelerate LSTM computations, such as matrix multiplications and element-wise operations, making real-time execution of the SEQ2SEQ model highly feasible. Efficient batching and parallel processing further enhance throughput, allowing continuous data streams to be processed within the satellite's real-time communication constraints.

Although the Intel Tiger Lake UP3 SoC is designed for power efficiency, continuous deep learning operations can be power-intensive. Nonetheless, the low complexity of the SEQ2SEQ model helps keep power consumption within acceptable limits for modern LEO satellites. The model's minimal memory requirements also ensure that the 4 GB of available memory is sufficient, reducing the need for frequent memory swaps and maintaining efficient operation.

VI. NUMERICAL RESULTS

A. *Spectrum sensing at LEO satellite*

This section presents the numerical results that validate the theoretical analysis of spectrum sensing at LEO satellite. The simulation on Doppler shift at LEO satellite is conducted using the Matlab Satellite Communication Toolbox. The system is configured with Inmarsat-4 F1 as the GEO satellite and Iridium-NEXT 145 as the LEO satellite. The key orbital parameters' values are detailed in Table II. The satellite orbit datasets in the Toolbox are sourced from Space-Track [38]. In addition, the Monte Carlo method is employed in this section, where a dataset of 16,000 GEO signals is generated. These signals span various SNR values ranging from -20 dB to 10 dB.

TABLE II: Orbital parameters used for simulation.

Parameter	**Inmarsat-4 F1**	**Iridium-NEXT 145**
Orbital period (hr)	24	1.673
Semi-major axis (km)	42,164	7,155
Eccentricity	0.00028	0.00026
Inclination (degree)	3.880	86.394
Right ascension of ascending node (degree)	58.28	151.546
Argument periapsis (degree)	22.984	83.843
Mean anomaly (degree)	200.58	0.105

Fig. 9 illustrates the Doppler shift experienced by LEO satellite during its three orbits. The numerical results obtained from (22) correspond to the analytical data. The period of unavailability of data occurs when LEO satellite orbits outside the transmission range of GEO satellite. Depending on the actual position and velocity of LEO satellite, the experienced Doppler shift varies, reaching a maximum value of ±38 kHz. Furthermore, the results validate the analysis of Doppler shift characterization, as there is no significant deviation between the simulation and analytical outcomes, and the Doppler shift adheres to the Doppler S-curve.

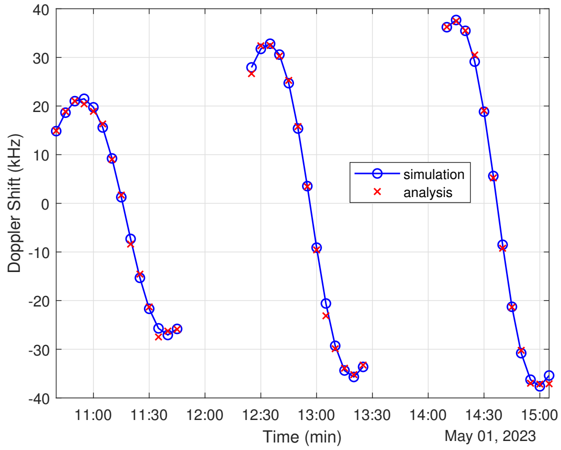

Fig. 9: Doppler shift observed at LEO satellite, during an orbit cycle of GEO satellite.

Fig. 10 depicts the distribution of CACFs and test statistics for 1000 GEO signals at a SNR of 0 dB. The PDFs derived in

Section IV-B are represented by the red curves. Both CACFs for the two test cases conform to a Gaussian distribution, while the test statistics adhere to a Chi-squared distribution with two degrees of freedom. In Fig. 10b, the red curve validates the analytical results, illustrating the PDF of $|\hat{R}_y^{\alpha}|^2|\mathcal{H}_{0,\iota}$ as per (27). Similarly, Fig. 10d confirms the analytical findings, with the red curve depicting the PDF of $|\hat{R}_y^{\alpha}|^2|\mathcal{H}_{1,\iota}$ as per (33). It is noteworthy that the latter follows a non-central Chi-squared distribution with a noncentrality parameter $\lambda = 1.527$.

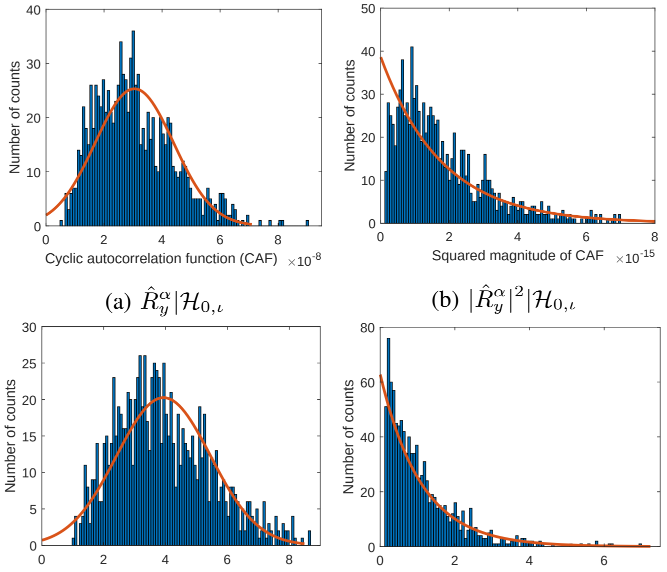

(a) $\hat{R}_y^{\alpha}|\mathcal{H}_{0,\iota}$

(b) $|\hat{R}_y^{\alpha}|^2|\mathcal{H}_{0,\iota}$

(c) $\hat{R}_y^{\alpha}|\mathcal{H}_{1,\iota}$

(d) $|\hat{R}_y^{\alpha}|^2|\mathcal{H}_{1,\iota}$

Fig. 10: Distribution of the CACF and test statistics of 1000 GEO signals at SNR = 0 dB.

The performance of the sensing system is illustrated in Figs. 11 and 12. Fig. 11 presents a comparison between theoretical and simulated detection probability curves as a function of SNR under varying false alarm probability conditions. It demonstrates that the detection probability can surpass 90% for SNR values greater than -7 dB and exceed 50% for SNR values greater than -15 dB, provided that the false alarm probability is at least 20%. This notable performance in the low SNR range is attributed to the robustness of the cyclostationary-based detection method to noise. Fig. 12 displays the Receiver Operating Characteristic (ROC) curves, depicting the relationship between misdetection probability and false alarm probability for different SNR levels. For SNR values of -6 dB and -2 dB, the ROC curves indicate that the proposed sensing algorithm exhibits good sensitivity, with very low misdetection probability, compared to its specificity in terms of false alarm probability. However, for lower SNR levels represented by other curves, a noticeable increase in both false alarm probability and misdetection probability is observed as the classification threshold becomes less strict. These findings suggest that the sensitivity of the sensing algorithm is notably lower compared to its specificity at lower SNR levels.

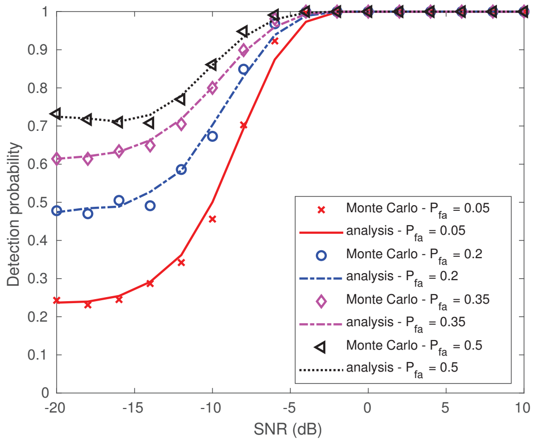

Fig. 11: Detection probability for different SNR.

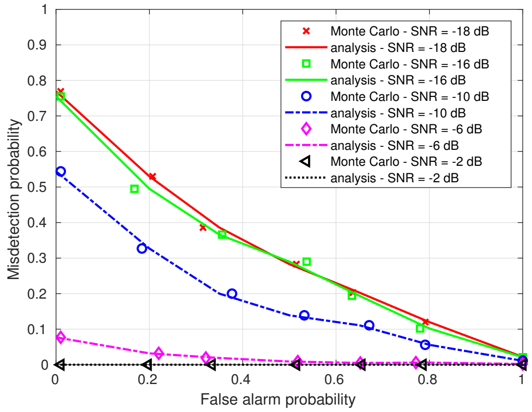

Fig. 12: ROC curves for different SNR.

B. Spectrum prediction based on REM

1) Dataset details: The REM data is compiled from our measurement data of downlink signals of Inmarsat-4 F1 as described in Section II. We compiled four local REMs for two LEO satellites positioned in the Sydney beam and Adelaide beam under the GEO frequency reuse scheme of 4-color and 2-color. These REMs serve as the ground truth during the training and validation processes.

The dataset is generated using a sliding window method with a window length of n_t based on REM. In Fig. 7, the network produces predictive states for all beams within the transmission range of S_{L_1} at time-slot ζT_S. Simultaneously, the satellite observes a known vector at ζT_S slot, which is selected as the label for that specific sample. This process involves advancing the sliding window by one time-slot, creating a sample that contributes to the neural network's dataset. In the event of beams changing within the transmission range of S_{L_1} in the next time-slot, a new set of data for a window is obtained from the REM. This highlights the importance of keeping the REM up to date through collaboration with neighboring satellites.

2) Simulation setup: The two neural networks undergo data training and testing using four REMs, each comprising

4000 time-step data points. Parameters from Inmarsat-4 F1 and Iridium-NEXT 145 are employed to represent the GEO and LEO satellites respectively, resulting in a coverage of 19 GEO spot beams within the LEO transmission range. Table III provides a summary of the key hyperparameters utilized for simulation.

TABLE III: Hyperparameters used for simulation.

Network	**Parameter**	**Value**
Common	No. epochs	1000
	Batch size	32
	No. beams of interest	19
	Learning rate	0.001
	Optimizer	Adam
	Loss function	Binary cross-entropy
SEQ2SEQ	Mem. blocks per LSTM unit	2
	No. LSTM units per layer	19
	No. neuron output layer - decoder	19
2DCNNLSTM	No. filter - conv. layer	64
	Kernel size - conv. layer	3 × 3
	Mem. blocks LSTM layer 1	100
	Mem. blocks LSTM layer 2	50
	No. neuron output layer - decoder	19

3) Simulation results: Figs. 13 and 14 illustrate the performance of the two networks across different numbers of historical data required for prediction. The comparison is conducted using both Sydney and Adelaide REMs under a 4-color frequency reuse scheme. In Fig. 13, the detection probability improves for all cases as the number of historical data n_t increases. Beyond $n_t > 8$ time-steps, the detection probability shows slight variation, remaining below 3%. Similarly, in Fig. 14, the false alarm probability demonstrates analogous behavior. The overall performance of the proposed SEQ2SEQ method demonstrates better detection probability across all scenarios compared to the 2DCNN-LSTM model. For $n_t < 5$ time-steps, the benchmark outperforms the proposed SEQ2SEQ model in terms of false alarm probability. This is because the SEQ2SEQ model requires more data to accurately capture the spectral and temporal dependencies of GEO beam statuses. However, as the historical data increases to 8 time steps and beyond, the SEQ2SEQ model's performance improves, surpassing the benchmark in false alarm probability and achieving more efficient spectrum usage compared to the 2DCNNLSTM benchmark. Notably, at $n_t = 8$, the proposed SEQ2SEQ network outperforms the benchmark by 18% in terms of false alarm probability, while exhibiting computational complexity ten times lower than that of the benchmark.

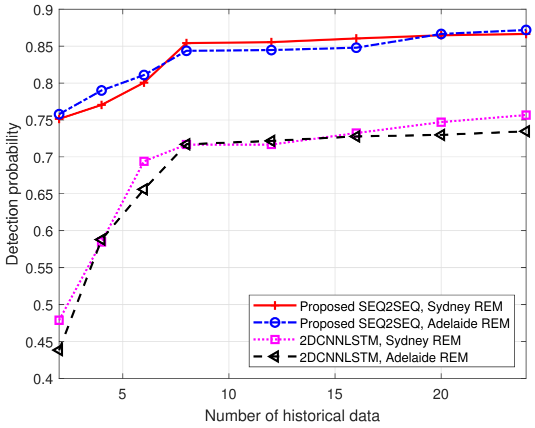

Fig. 13: Detection probability under different number of historical data with 4-color frequency reuse GEO beams.

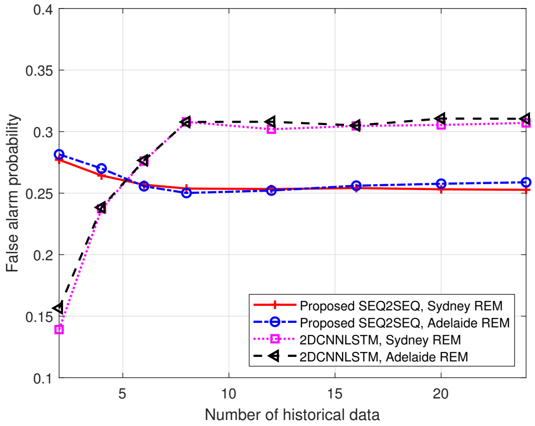

Fig. 14: False alarm probability under different number of historical data with 4-color frequency reuse GEO beams.

The SEQ2SEQ algorithm's performance advantage is attributable to its efficient architecture, which consists of an encoder-decoder structure with LSTM layers and dense networks. This design allows the SEQ2SEQ model to capture sequential dependencies and make predictions effectively with fewer computational resources. Specifically, the SEQ2SEQ model's direct sequence-to-sequence learning approach eliminates the need for complex convolutional processing, which is required by the 2DCNNLSTM model. This simplicity results in a significant reduction in computational overhead, as evidenced by the ten-fold decrease in complexity (with $n_t = 8$ and $n_b = 19$). The 2DCNNLSTM model, on the other hand, involves a more complex processing pipeline. It begins with a 2D convolutional layer that analyzes spectral and temporal correlations, followed by a dense layer for reshaping the output into a format suitable for LSTM processing. This approach adds additional layers of computation and complexity, which contributes to the higher overall complexity of the model.

Fig. 15 presents the performance analysis of the proposed SEQ2SEQ network across varying numbers of memory blocks per LSTM unit. These results are obtained using eight historical data points and a 4-color frequency reuse scheme in Sydney REM. It is evident that the performance of the proposed network improves with an increase in the number of memory blocks per LSTM unit. However, this enhancement is accompanied by a rise in computational complexity, given that the proposed network incorporates $4n_b$ LSTM units.

Figs. 16 and 17 depict the performance of the proposed network under both 4-color and 2-color frequency reuse schemes for Sydney and Adelaide REMs. These results are obtained using a network architecture featuring 2 memory blocks per LSTM unit. We observe superior performance,

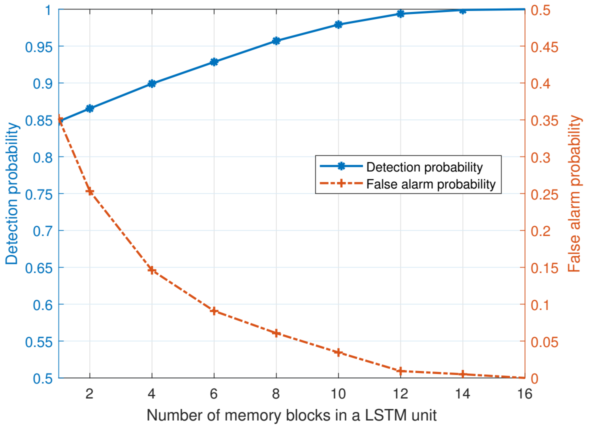

Fig. 15: Performance of the proposed SEQ2SEQ network under different number of memory blocks per LSTM unit, $n_t = 8$, 4-color frequency reuse scheme, Sydney REM.

with an average of 15% higher detection probability under the 4-color frequency reuse scheme. This improvement can be attributed to the higher correlation in the activity patterns of beams under the 4-color frequency reuse scheme compared to the 2-color frequency reuse scheme.

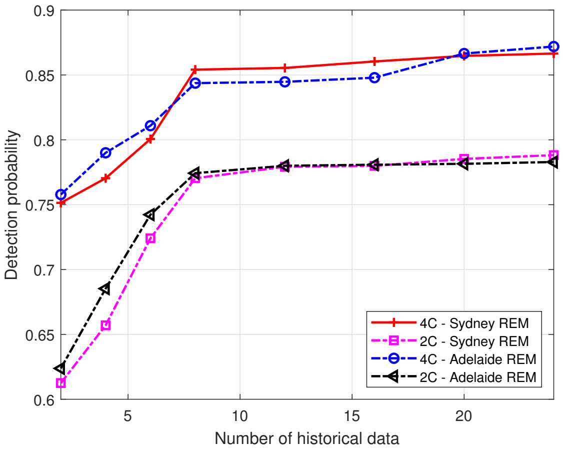

Fig. 16: Detection probability under different number of historical data with 4-color and 2-color frequency reuse schemes of the proposed SEQ2SEQ network.

To assess the feasibility of implementing the proposed spectrum prediction algorithm, we used a laptop with an Intel Core i5-8250U CPU at 1.6 GHz and 4 GB of memory to emulate the Intel Tiger Lake SoC found on-board LEO satellites [37]. The i5-8250U, with its 4 cores and 8 threads, offers performance comparable to the Tiger Lake UP3 SoC. However, its integrated graphics, while more advanced than previous generations, still fall short of the Tiger Lake SoC's GPGPU with 96 Execution Units. Additionally, the Tiger Lake UP3's 4 GB of memory is optimized with advanced management techniques that the i5-8250U cannot fully replicate. Consequently, while the i5-8250U provides valuable insights into performance trends, it does not fully capture the enhanced GPU performance, memory optimization, and overall efficiency of the Tiger Lake UP3 SoC.

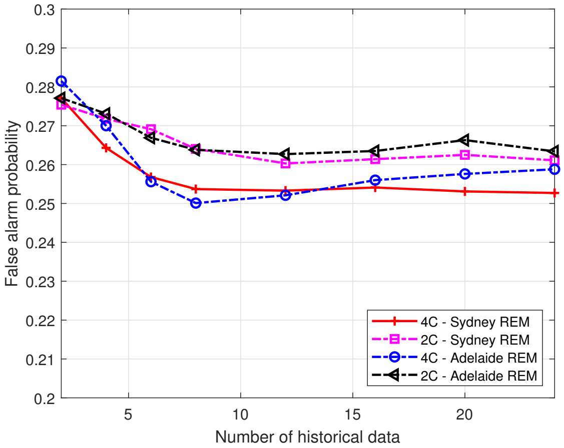

Fig. 17: False alarm probability under different number of historical data with 4-color and 2-color frequency reuse schemes of the proposed SEQ2SEQ network.

The execution time for the proposed SEQ2SEQ under different number of historical data n_t is shown in Table IV.

TABLE IV: Computation delay of the proposed spectrum prediction algorithm with on-board LEO satellite resources under various number of historical data.

Number historical data	4	8	12	16	20	24
Computation delay (ms)	0.91	1.31	1.72	2.12	2.53	2.93

With the current configuration, it takes 145 seconds for the LEO satellite to pass through a single GEO beam. Given that each time-slot lasts 1 second and the sensing window occupies 10% of that time, the proposed algorithm's computation delay of under 3 milliseconds accounts for less than 10% of the sensing window. This efficient use of time allows for extended opportunities for secondary transmission through spectrum prediction.

VII. CONCLUSION

In this paper, we first investigated the feasibility of conducting sensing on LEO satellites by analyzing real data captured from Inmarsat-4 F1 L-band downlink at two distinct locations: Sydney and Adelaide, Australia. Subsequently, we introduced a novel REM construction protocol tailored for LEO satellites within cognitive GEO-LEO satellite IoT networks. This protocol enables REM construction through collaboration among neighboring LEO satellites, if available, or through the operation of a single LEO satellite. Moreover, it takes into account the frequency reuse scheme of GEO satellite. Our REM construction approach leverages cyclostationary-based sensing at LEO satellites, serving the dual purpose of REM construction and Doppler shift estimation. We studied the characteristics of Doppler shift experienced by LEO satellites and estimated it by extracting features from sensed GEO signals. Following REM construction, LEO satellites utilize deep learning techniques to predict GEO spectrum occupancy, enabling them to access the spectrum without the need for additional sensing. This approach optimizes secondary spectrum utilization for LEO satellite IoT networks. We proposed a deep learning neural network architecture based on sequence-to-sequence model, designed for spectrum prediction. Notably, our proposed network demonstrated superior performance compared to convolutional LSTM networks, achieving this with lower computational complexity.

REFERENCES

[1] D. C. Nguyen, M. Ding, P. N. Pathirana, and et.al., "6G internet of things: A comprehensive survey," *IEEE Internet Things J.*, vol. 9, no. 1, pp. 359–383, 2022.

[2] M. A. Ferrag, O. Friha, B. Kantarci, and et.al., "Edge learning for 6G-enabled internet of things: A comprehensive survey of vulnerabilities, datasets, and defenses," *IEEE Commun. Surveys Tuts. Mag.*, vol. 25, no. 4, pp. 2654–2713, 2023.

[3] S. Wang and Q. Li, "Satellite computing: Vision and challenges," *IEEE Internet Things J.*, vol. 10, no. 24, pp. 22 514–22 529, 2023.

[4] Q. T. Ngo, Z. Tang, B. Jayawickrama, and et.al., "Timeliness of information in 5G non-terrestrial networks: A survey," *IEEE Internet Things J.*, vol. 11, no. 21, pp. 34 652–34 675, 2024.

[5] Q. T. Ngo, B. A. Jayawickrama, Y. He, and E. Dutkiewicz, "Multi-agent DRL-based RIS-assisted spectrum sensing in cognitive satellite–terrestrial networks," *IEEE Wireless Commun. Lett.*, vol. 12, no. 12, pp. 2213–2217, 2023.

[6] R. Yao, Y. Yu, P. Wang, and et.al., "Green integrated cooperative spectrum sensing for cognitive satellite terrestrial networks," *IET Commun.*, vol. 17, no. 14, pp. 1665–1682, 2023.

[7] J. Hu, G. Li, D. Bian, S. Shi, R. Ge, and L. Gou, "Energy-efficient cooperative spectrum sensing in cognitive satellite terrestrial networks," *IEEE Access*, vol. 8, pp. 161 396–161 405, 2020.

[8] M. Mueck, Y. He, B. Jayawickrama and E. Dutkiewicz, "Methods and devices for user detection in spectrum sharing," (Jun 2020). U.S. Patent US10681558B2. [Online]. Available: https://patents.google.com/patent/US10681558B2/en

[9] B. A. Jayawickrama, E. Dutkiewicz, M. Mueck, and Y. He, "On the usage of geolocation-aware spectrum measurements for incumbent location and transmit power detection," *IEEE Trans. Veh. Technol.*, vol. 65, no. 10, pp. 8177–8189, 2016.

[10] Q. T. Ngo, B. Jayawickrama, Y. He, and et.al., "Optimizing spectrum sensing in cognitive GEO-LEO satellite networks: Overcoming challenges for effective spectrum utilization," *Preprint TechRxiv*, 2024.

[11] Y. Wang, X. Ding, and G. Zhang, "A novel dynamic spectrum-sharing method for GEO and LEO satellite networks," *IEEE Access*, vol. 8, pp. 147 895–147 906, 2020.

[12] Q. Ngo, B. Jayawickrama, Y. He, and E. Dutkiewicz, "Machine learning-based cyclostationary spectrum sensing in cognitive dual satellite networks," in *Proc. IEEE Int. Sympos. Commun. Inf. Tech. (ISCIT)*, 2023, pp. 1–6.

[13] H. M. Furqan, M. S. Solaija, H. Türkmen, and H. Arslan, "Wireless communication, sensing, and REM: A security perspective," *IEEE Open J. Commun. Society*, vol. 2, pp. 287–321, 2021.

[14] M. Höyhtyä, A. Mämmelä, X. Chen, and et.al., "Database-assisted spectrum sharing in satellite communications: A survey," *IEEE Access*, vol. 5, pp. 25 322–25 341, 2017.

[15] H. Wang, R. Ren, D. Qu, and G. Zhang, "A radio environment mapping based spectrum awareness for cognitive space information network with GEO and LEO coexistence," in *Proc. Int. Conf. Wireless Commun. Signal Process. (WCSP)*, 2020, pp. 654–659.

[16] K. Weththasinghe, N. Clark, Q. T. Ngo, and et.al., "L-band spectral opportunities for cognitive GEO-LEO dual satellite networks," in *Proc. IEEE Int. Sympos. Commun. Inf. Tech. (ISCIT)*, 2023, pp. 1–5.

[17] L. Daniel, S. Hristov, X. Lyu, and et.al., "Design and validation of a passive radar concept for ship detection using communication satellite signals," *IEEE Trans. Aerospace and Electronics Syst.*, vol. 53, no. 6, pp. 3115–3134, 2017.

[18] J. Perez-Trufero, B. G. Evans, M. Dervin, and C. Baudoin, "High throughput satellite system with Q/V-band gateways and its integration with terrestrial broadband communication networks," in *Proc. AIAA Int. Commun. Satellite Syst. Conf.*, 2014, pp. 4384–4390.

[19] M. Mathpal, "A landmark based shortest path detection by using A* and Haversine formula," *Int J Recent Innov Trends Comput Commun*, vol. 6, no. 7, pp. 98–101, 2018.

[20] Inmarsat, "I-4 Coverage," May 2020. [Online]. Available: www.inmarsat.com/inmarsat/document.

[21] International Civil Aviation Organization, "Manual for ICAO Aeronautical Mobile Satellite (Route) Service, Part 2-Iridium, Draft v4.0," Mar 2007. [Online]. Available: www.icao.int/ACP-WG-M-Iridium-8

[22] M. Werner, A. Jahn, E. Lutz, and A. Bottcher, "Analysis of system parameters for LEO/ICO-satellite communication networks," *IEEE J. Select. Areas Commun.*, vol. 13, no. 2, pp. 371–381, 1995.

[23] Q. T. Ngo, K. T. Phan, A. Mahmood, and W. Xiang, "Physical layer security in IRS-assisted cache-enabled satellite communication networks," *IEEE Trans. Green Commun. Netw.*, vol. 7, no. 4, pp. 1920–1931, 2023.

[24] Q. T. Ngo, K. Phan, A. Mahmood, and W. Xiang, "Hybrid IRS-assisted secure satellite downlink communications: A fast deep reinforcement learning approach," *IEEE Trans. Emerg. Top. Comput. Intell.*, vol. 8, no. 4, pp. 2858–2869, 2024.

[25] R. Ge, D. Bian, K. An, J. Cheng, and H. Zhu, "Performance analysis of cooperative nonorthogonal multiple access scheme in two-layer GEO/LEO satellite network," *IEEE Syst. J.*, vol. 16, no. 2, pp. 2300–2310, 2022.

[26] E. Trachtman, "Broadband for a mobile planet," in *Proc. Int. Workshop B3G/4G Satellite Commun.*, 2006, Seoul, pp. 1–5.

[27] A. Dandawate and G. Giannakis, "Statistical tests for presence of cyclostationarity," *IEEE Trans. Signal Process.*, vol. 42, no. 9, pp. 2355–2369, 1994.

[28] S. Shamsunder, G. Giannakis, and B. Friedlander, "Estimating random amplitude polynomial phase signals: a cyclostationary approach," *IEEE Trans. Signal Process.*, vol. 43, no. 2, pp. 492–505, 1995.

[29] C. An and H.-G. Ryu, "Compensation systems and performance comparison of the very high doppler frequency," in *Proc. IEEE Int. Conf. Commun. Netw.*, 2020, pp. 1–4.

[30] W. Pritchard, H. Suyderhoud, and R. Nelson, *Satellite communication systems engineering*, 2nd ed. Prentice Hall, 1993, vol. 1.

[31] J. Crestel, B. Emile, M. Guitton, and D. Menard, "A doppler frequency estimate using the instantaneous frequency," in *Proc. IEEE Int. Conf. Digi. Signal Process.*, vol. 2, 1997, pp. 777–780.

[32] K. Cho, B. van Merrienboer, C. Gulcehre, and et.al., "Learning phrase representations using RNN encoder-decoder for statistical machine translation," in *Proc. Conf. Empirical Methods Natural Language Process.*, 2014, pp. 75–80.

[33] I. Sutskever, O. Vinyals, and Q. Le, "Sequence to sequence learning with neural networks," *Advances Neural Inf. Process. Syst.*, vol. 27, pp. 147–159, 2014.

[34] J. Van Der Westhuizen and J. Lasenby, "The unreasonable effectiveness of the forget gate," *arXiv preprint arXiv:1804.04849*, pp. 895–906, 2018.

[35] B. S. Shawel, D. H. Woldegebreal, and S. Pollin, "Convolutional LSTM-based long-term spectrum prediction for dynamic spectrum access," in *Proc. European Signal Process. Conf.*, 2019, pp. 1–5.

[36] H. He, W. Yuan, Y. Hou, S. Chen, X. Jiang, R. Zhu, and J. Yang, "Onboard processing aided transmission delay minimization for LEO satellite networks," *IEEE Trans. Commun.*, pp. 1–15, 2024.

[37] NASA, "State-of-the-art of small spacecraft technology," February 2024. [Online]. Available: https://www.nasa.gov/smallsat-institute/sst-soa/small-spacecraft-avionics/.

[38] Space-Track, "Satellite catalog," April 2024. [Online]. Available: https://space-track.org/catalog.

QUYNH TU NGO (Senior Member, IEEE) received a B.Sc. in Electrical Engineering (Magna Cum Laude) from California State University Los Angeles, USA, in 2013; an M.Sc. in Telecommunications from Vietnam National University - University of Sciences, Vietnam, in 2016; and a Ph.D. in Computer Science from La Trobe University, Australia, in 2023. She is currently a Postdoctoral Research Fellow at the School of Electrical and Data Engineering, University of Technology Sydney, Australia. Her research interests include satellite communications, IoT networks, intelligent non-terrestrial networks, and machine learning in wireless communications and networking.

Beeshanga Jayawickrama (Senior Member, IEEE) received the B.E. degree (Hons. I) in Telecommunications Engineering and the Ph.D. degree in Electronic Engineering from Macquarie University, Australia, in 2011 and 2015, respectively. He is currently affiliated as a Visiting Fellow at University of Technology Sydney, Australia. He was extensively involved in spectrum sensing and interference mitigation research for spectrum access systems. His research interests include non-terrestrial networks, 5G/6G, cognitive radio, and signal processing.

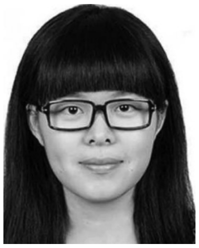

Ying He (Senior Member, IEEE) received the B.Eng. degree in Telecommunications Engineering from Beijing University of Posts and Telecommunications, China, in 2009, and the Ph.D. degree in Telecommunications Engineering from the University of Technology Sydney, Australia, in 2017. She is currently a Senior Lecturer with the School of Electrical and Data Engineering, University of Technology Sydney. Her research interests are physical layer algorithms in wireless communication with machine learning, vehicular communication, spectrum sharing and satellite communication.

Eryk Dutkiewicz (Senior Member, IEEE) received his B.E. degree in Electrical and Electronic Engineering in 1988 and his M.Sc. degree in Applied Mathematics in 1992 from the University of Adelaide, Australia, and his Ph.D. in Telecommunications from the University of Wollongong, Australia, in 1996. His industry experience includes management of the Wireless Research Laboratory at Motorola in early 2000's. Prof. Dutkiewicz is currently Associate Dean International in the Faculty of Engineering and IT at University of Technology Sydney, Australia. He also holds a professorial appointment at Hokkaido University in Japan. His current research interests cover 5G/6G and IoT networks.